Supplementary Information for

Orientation-modulated oxygen evolution reaction in epitaxial $SrRuO_3$ films

Shencheng Pan[a], Lianjin Wei[a], Junlong Xie[a], Zhenjie Lu[a], Jiajia Yuan[a], Tian Tang[a], Leichao Meng[b], Xin Wang[a], Junwu Zhu[a], Yongsheng Fu[a,*]

[a] *Key Laboratory for Soft Chemistry and Functional Materials of Ministry of Education, Nanjing University of Science and Technology, Nanjing 210094, China*

[b] *Qinghai Provincial Key Laboratory of Nanomaterials and Technology, Qinghai Minzu University, Xi'ning 81007, China*

*Corresponding authors. E-mail: fuyongsheng@njust.edu.cn

Experimental Sections

Fabrication of SRO Thin Films with (001), (011), and (111) Orientations

The SRO-001, SRO-011, and SRO-111 thin films were fabricated on (001), (011), and (111) oriented $SrTiO_3$ (STO) substrates (AR. Hefei Kejing Materials Technology co., LTD), respectively, utilizing a combination of KrF excimer laser ablation and Pulsed Laser Deposition (PLD, λ = 248 nm, COMPexPro 201, co., LTD). The STO substrate was maintained at 700°C under a vacuum of less than 10^{-4} Pa during the deposition process. The laser irradiation was performed at a repetition rate of 2 Hz with a pulse energy density of 1.2 J/cm^2, while maintaining a target-to-substrate distance of 5.5 cm. Following deposition for 7 minutes, the films underwent in situ annealing for 20 minutes before cooling to room temperature. The film thickness, estimated to be approximately 20 nm, was determined based on a deposition rate of around 3 nm/minute. It is assumed that the films possess the same composition as the target material.

Electrochemical measurements

The evaluation of the electrochemical properties was conducted using a standard three-electrode setup connected to an Auto-Lab electrochemical workstation (PGSTAT302N, Switzerland). A carbon rod was employed as the counter electrode while the Hg/HgO electrode was used as the reference electrodes in 1 M KOH solution (AR, Sinopharm group chemical reagent co. LTD). To ensure the accuracy of the data, we refresh the internal solution of the reference electrode with KOH standard solution before testing. The SRO thin films with different orientations grown on STO as the working electrodes. The linear sweep voltammetry (LSV) curves for OER were measured at the scan rate of 5mV/s with 95% iR compensation, and the iR compensation was automatically corrected by the software. The cyclic voltammogram (CV) curves of electrochemically active surface areas (ECSA) were measured with different scan rates of 20, 40, 60, 80, 100, 120, and 150 mV/s. All the potentials in this paper were measured with the Hg/HgO electrode (with 1 M KOH, pH = 14), and then transformed to the reversible hydrogen electrode (RHE) using the conversion formula: $E_{RHE} = E_{Hg/HgO} + 0.0591pH + 0.098$. To ensure the accuracy of the data, we refresh the internal solution of the reference electrode with KOH standard solution before testing.

SECM Characterization

The SECM experiments were performed using a four-electrode system controlled by a double potentiostat (Guangdong Dynechem Electronics Technology Co., Ltd., China). A platinum wire with a diameter of 25 μm is sealed in a glass capillary with a diameter of 225 μm to serve as the SECM probe electrode (RG value = 9). For the feedback mode, the electrolyte is a mixed solution of 0.01 M $K_3[Fe(CN)_6]$ and 0.1 M KCl (AR, Sinopharm group chemical reagent co. LTD). For the sample generation-tip collection (SG-TC) mode, the electrolyte is a 1 M KOH

solution. The counter electrode is carbon rod and the reference electrodes is Hg/HgO.

The current data obtained from SECM was normalized using the following formula: Normalized Current = $\Delta i/\Delta i_{Max}$

Where Δi is the actual current value at each sampling point minus the minimum current value across the entire region, and Δi_{Max} is the maximum Δi value within the sampling area.

Characterization

The structures of the SRO films were measured by X-ray diffraction (XRD, PANalytical Empyrean/X'pert MRD, Resolution 0.0001°) using Cu Kα radiation, including θ-2θ line scan and reciprocal space mapping (RSM). Scanning electron microscopy (SEM) images and energy-dispersive X-ray spectroscopy (EDS) elemental mapping images were collected on a JSM-7800F Prime. The composition and binding energy of the films were characterized by X-ray photoelectron spectroscopy (XPS, VG Scientific, ESCALAB-250, Energy resolution 0.45 eV/(Ag $3d_{5/2}$)) with Al-anode X-ray source (Al K_α $h\nu$ =1486.6 eV). The binding energies were calibrated with respect to the C1s peak (284.8 eV), derived from hydrocarbons absorbed on the surface of the film. The magnetic hysteresis loops were measured using a Physical Property Measurement System (PPMS) model: LakeShore 7404.

Computational Details

All spin-polarized density functional theory (DFT) calculations were carried out with Vienna ab initio simulation package (VASP). The exchange and correlation effects were taken into account using the generalized gradient approximation (GGA) method with Perdew-Burke-Ernzerhof (PBE) functionals[1-3]. The highly correlated Ru 4d orbitals were described using the Hubbard U calculation, and the value of U-J was set to 2.4 for Ru[4]. The weak interaction in

the system was described using the DFT-D3 correction[5]. The plane wave cutoff energy was set at 500 eV, the energy and force convergence criteria were set at 10^{-5} eV and 0.03 eV/Å. For Brillouin zone integration, the k-point grids used in surface and density of states (DOS) calculations are listed in **Table 1**. The thickness of the vacuum layer was established as greater than 20 Å for the calculations, ensuring the elimination of any impact from neighboring systems.

Orientation	001	011	111
k-point grids for Surface	3×3×1	3×2×1	3×3×1
k-point grids for DOS	9×9×1	9×6×1	9×9×1

The surface formation energy of SRO thin films for each growth orientation can be obtained using the formula denoted as S1:

$$\gamma = (E_{slab} - N \cdot E_{bulk}) / 2A \qquad \text{Eqn. S1}$$

In this context, γ represents the surface formation energy, E_{slab} represents the total energy obtained from DFT calculations of the surface, N denotes the number of atoms in the surface cell, E_{bulk} signifies the average energy per atom in the bulk material, and A represents the surface area of the surface model.

The OER process could occur in the following four-electron pathways (Eqn. S2-S5):

$$H_2O + * \rightarrow *OH + H^+ + e^- \quad (\Delta G_1) \qquad \text{Eqn. S2}$$

$$*OH \rightarrow *O + H^+ + e^- \quad (\Delta G_2) \qquad \text{Eqn. S3}$$

$$*O + H_2O \rightarrow *OOH + H^+ + e^- \quad (\Delta G_3) \qquad \text{Eqn. S4}$$

$$HOO * \rightarrow O_2 + * + H^+ + e^- \quad (\Delta G_4) \qquad \text{Eqn. S5}$$

where the * stands for the catalytic active site on the surface and the $\Delta G_1 - \Delta G_4$ represent the Gibbs free energies of the four reaction steps. The ΔG can be calculated by using the Eqn. S6:

$$\Delta G = \Delta E + \Delta ZPE - T\Delta S \quad \text{Eqn. S6}$$

where the ΔE was obtained from the DFT energy of structural relaxation. ΔZPE and ΔS were the change of zero-point energies (ZPE) and entropy. The temperature (T) was set to 298.15 K. The DFT energy of H_2O and H_2 were calculated in a boxes of 10 Å×10 Å×10 Å with the gamma point only. According to the computational hydrogen electrode model proposed by Nørskov et al[6]:

$$G(H^+) + (e^-) = 1/2\ G(H_2)(g) \quad \text{Eqn. S7}$$

The theoretical overpotential (η) of catalysts are defined in Eqn. S8:

$$\eta = \max(\Delta G_1, \Delta G_2, \Delta G_3, \Delta G_4)/e - 1.23\ \text{eV} \quad \text{Eqn. S8}$$

The DFT energy (E), zero-point energy (ZPE) and entropy contribution (-TS) correction of gas phase are as Table S1[7]:

Table S1. The DFT energy (E), zero-point energy (ZPE), entropy contribution (-TS) and free energy (G) of H_2O, H_2 and O_2.

Species	E_{DFT}	ZPE	-TS	G
H_2O (0.035 atm)	-14.221	0.566	-0.669	-14.325
H_2 (1 atm)	-6.770	0.265	-0.403	-6.908
O_2 (1 atm)	—	—	—	-9.912

The DFT energy (E), zero-point energy (ZPE) and entropy contribution (-TS) correction of adsorbed species were listed in Table S3-S8.

Table S3. The DFT energy (E), zero-point energy (ZPE) and entropy contribution (-TS) correction of adsorbed species for 001- RuO_2

001-RuO_2	E_{DFT}	ZPE	-TS
Slab	-336.68695	—	—
*OH	-347.56735	0.363991	-0.088152
*O	-342.88952	0.049144	-0.034765
*OOH	-352.06637	0.428601	-0.220521

Table S4. The DFT energy (E), zero-point energy (ZPE) and entropy contribution (-TS) correction of adsorbed species for 001- SrO

001-SrO	E_{DFT}	ZPE	-TS
Slab	-312.55343	—	—
*OH	-323.37719	0.305741	-0.170694
*O	-317.71584	0.04215	-0.090525
*OOH	-327.55343	0.384687	-0.178053

Table S5. The DFT energy (E), zero-point energy (ZPE) and entropy contribution (-TS) correction of adsorbed species for 011- SrRuO

001-SrRuO	E_{DFT}	ZPE	-TS
Slab	-456.99282	—	—
*OH	-469.30062	0.356181	-0.041694
*O	-465.08455	0.073483	-0.043767
*OOH	-472.4315	0.40904	-0.137437

Table S6. The DFT energy (E), zero-point energy (ZPE) and entropy contribution (-TS) correction of adsorbed species for 011- O_2

011- O_2	E_{DFT}	ZPE	-TS
Slab	-440.4448	—	—
*OH	-449.02971	0.280855	-0.045486
*O	-442.82982	0.015347	-0.088336
*OOH	-454.05668	0.404088	-0.285562

Table S7. The DFT energy (E), zero-point energy (ZPE) and entropy contribution (-TS) correction of adsorbed species for 111- Ru

111- Ru	E_{DFT}	ZPE	-TS
Slab	-530.2365	—	—
*OH	-540.91357	0.319196	-0.162852
*O	-538.54506	0.073783	-0.066233
*OOH	-546.37131	0.413371	-0.217047

Table S8. The DFT energy (E), zero-point energy (ZPE) and entropy contribution (-TS) correction of adsorbed species for 111- SrO_3

111- SrO_3	E_{DFT}	ZPE	-TS
Slab	-624.6064	—	—
*OH	-634.26596	0.293958	-0.184537
*O	-627.9442	0.041972	-0.06691
*OOH	-638.78705	0.390274	-0.308492

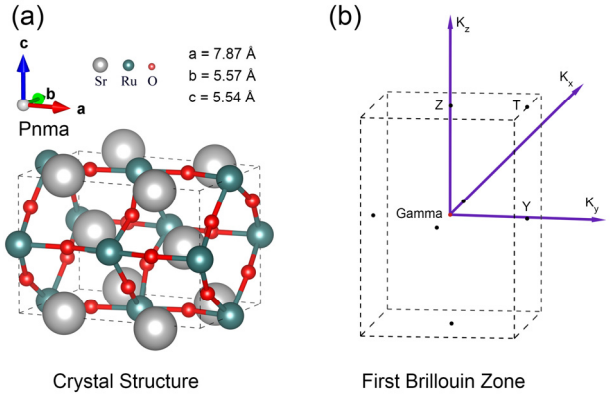

Figure S1: (a) Crystal structure diagram of SRO, (b) The corresponding k-points path along the high symmetry points in the first Brillouin zone

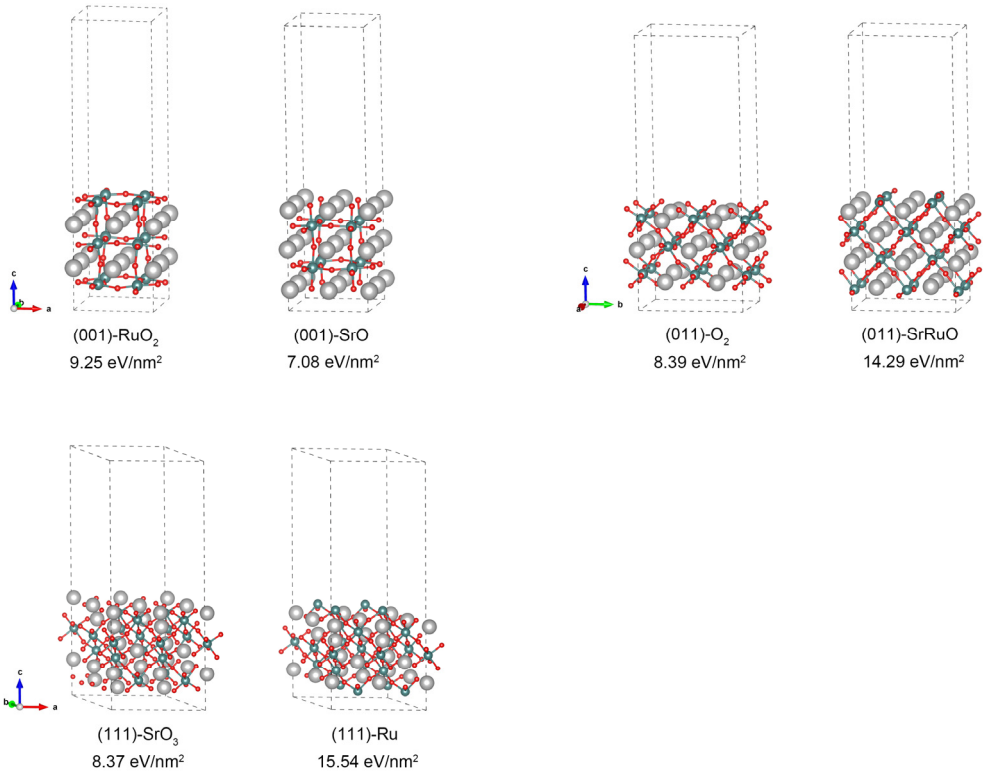

Figure S2: Possible surface atom terminations and their corresponding surface energies for three crystallographic orientations of SRO. The (001)-RuO_2 and (001)-SrO represent the two possible terminations of the SRO (001) surface, with the naming convention for the (011) and (111) surfaces following the same logic. The results reveal that all three growth orientations exhibit the lowest surface energy when terminated by non-Ru atoms.

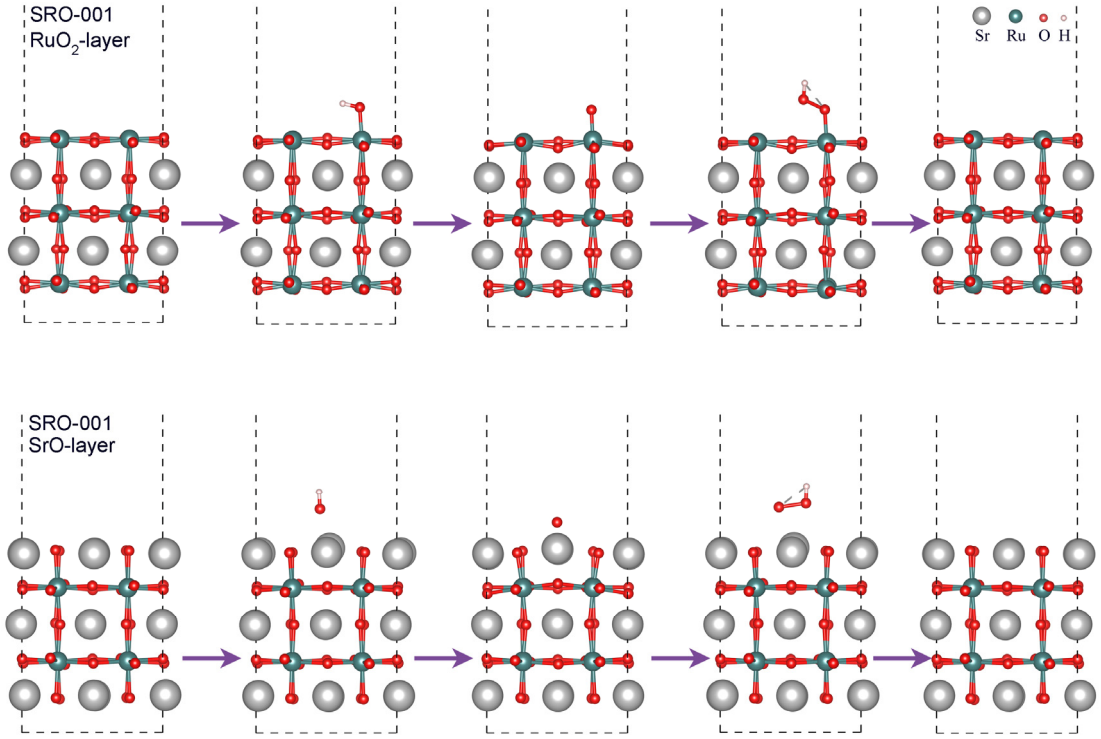

Figure S3: The schematic diagram of the OER process on SRO (001) surface.

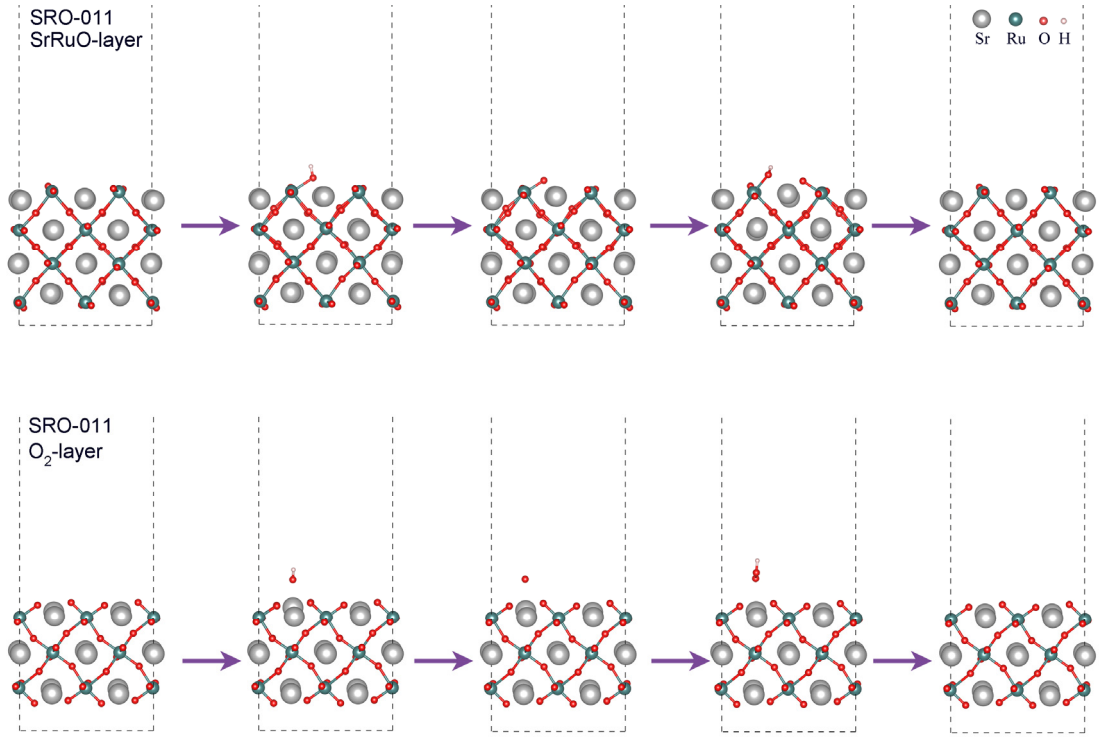

Figure S4: The schematic diagram of the OER process on SRO (011) surface.

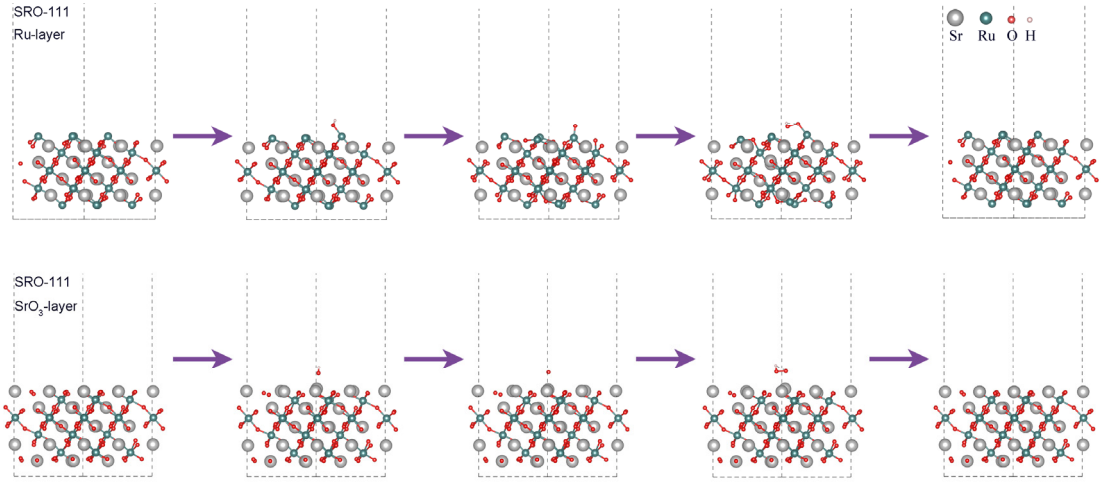

Figure S5: The schematic diagram of the OER process on SRO (111) surface.

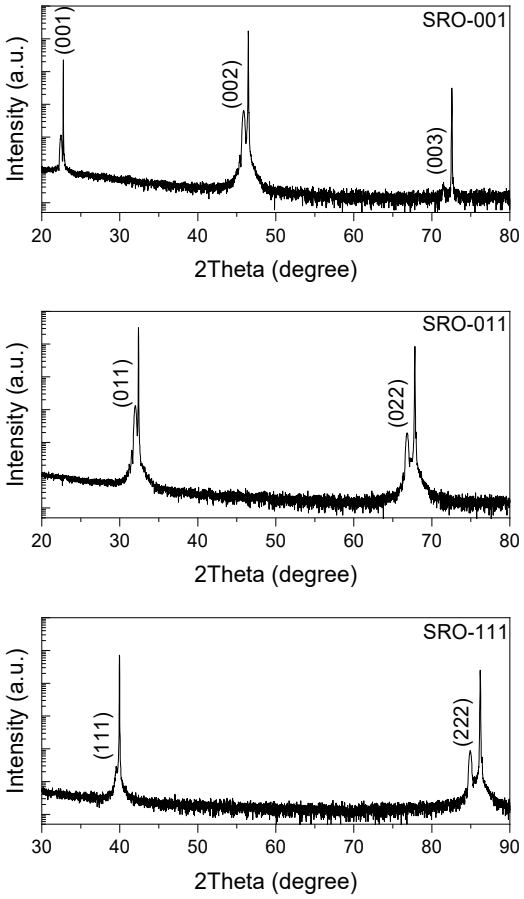

Figure S6: The wide range XRD 2theta-omega linear scans of the SRO-001, SRO-011, and SRO-111.

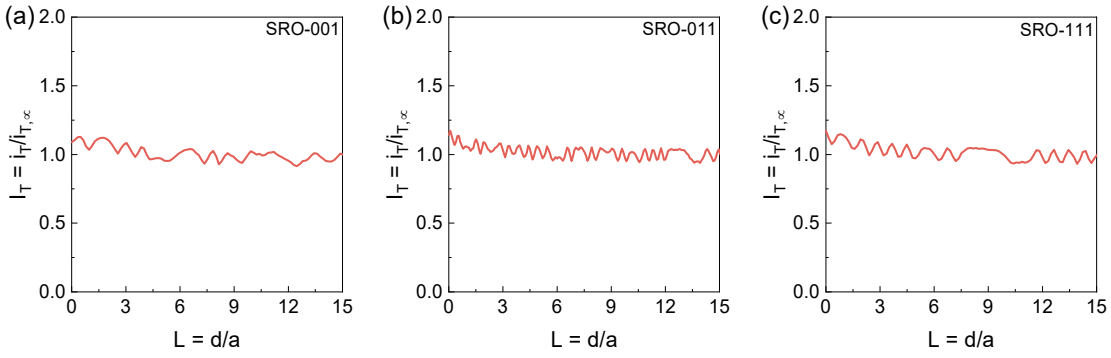

Figure S7: SECM tip approach curves (PACs) of SRO-001, SRO-011, and SRO-111.

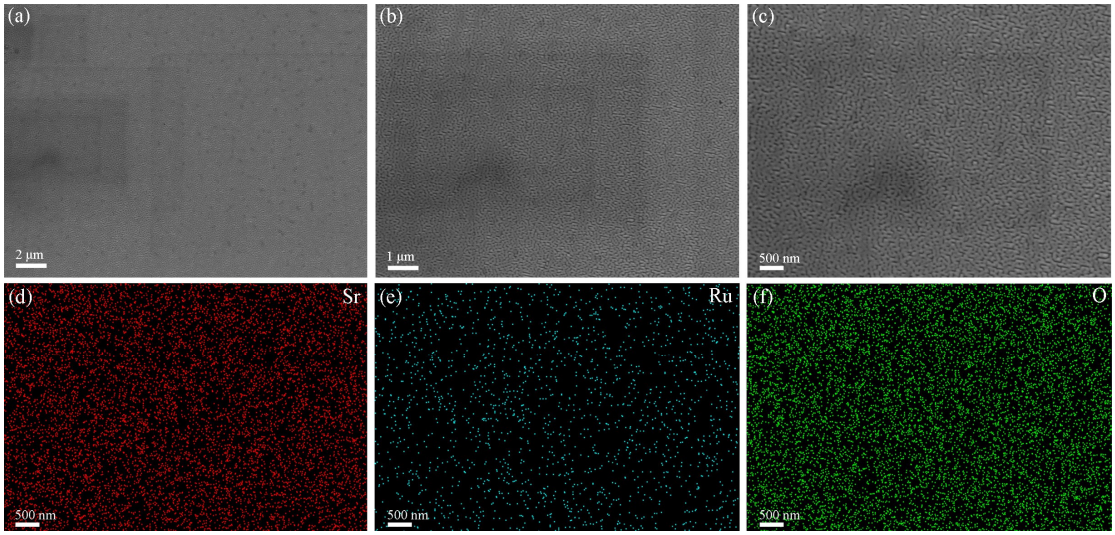

Figure S8: The SEM images and elements mapping of SRO-001.

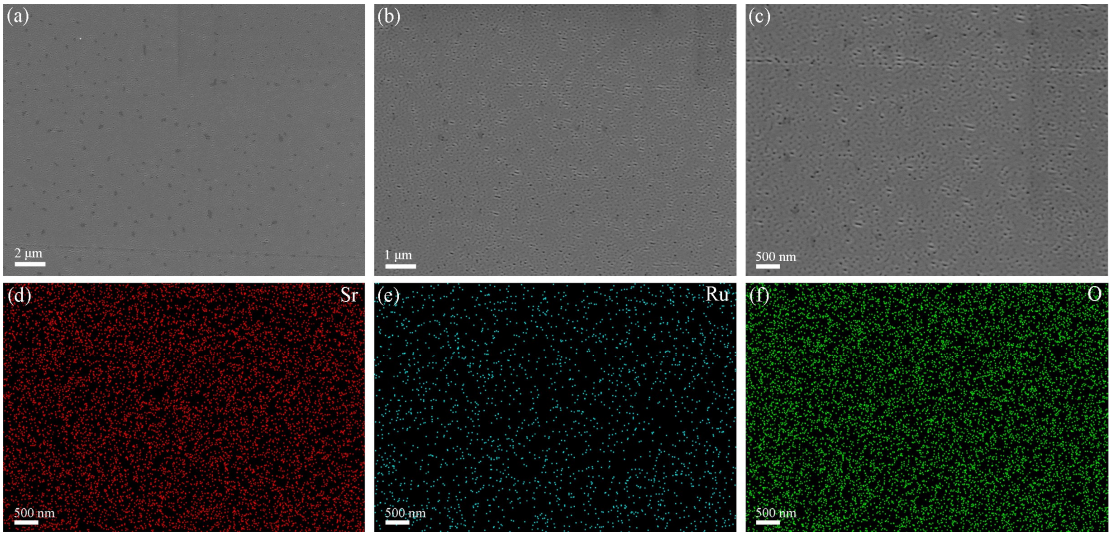

Figure S9: The SEM images and elements mapping of SRO-011.

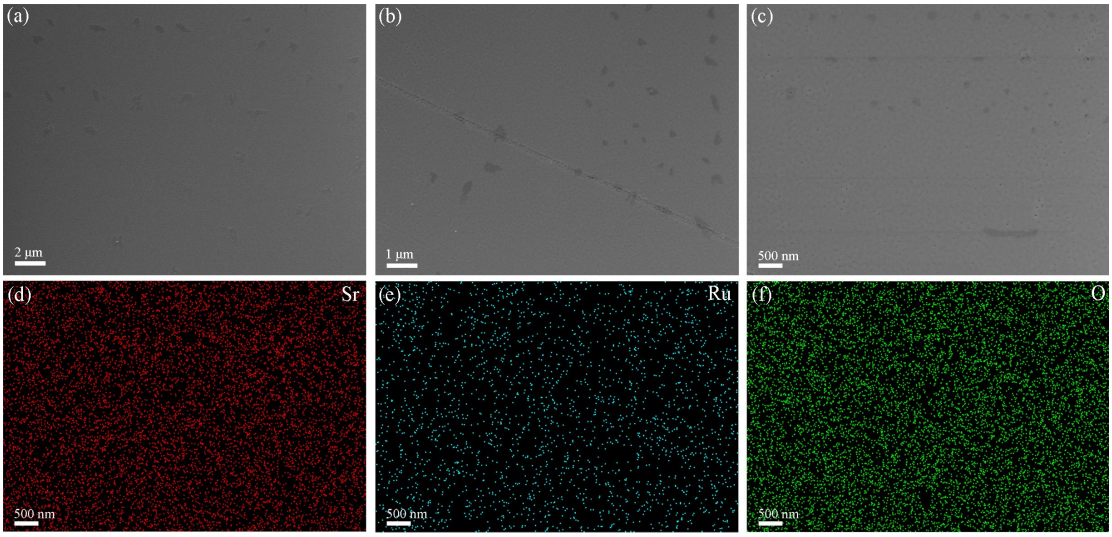

Figure S10: The SEM images and elements mapping of SRO-111.

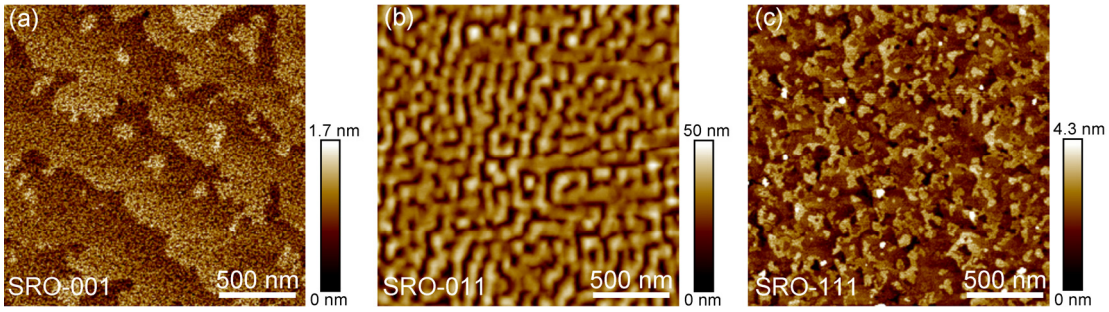

Figure S11: The AFM images and elements mapping of SRO-001, SRO-011, and SRO-111.

Surface roughness is known to impact OER catalytic activity by increasing the contact area between the catalyst and the electrolyte, which allows for a higher density of active sites. In our system, the SRO (001) surface, which exhibits greater roughness compared to the (011) and (111) surfaces, may contribute to improved OER performance. This enhancement is likely due to the increased availability of reaction sites, which can facilitate electron transfer and reaction kinetics, thereby potentially boosting catalytic efficiency.

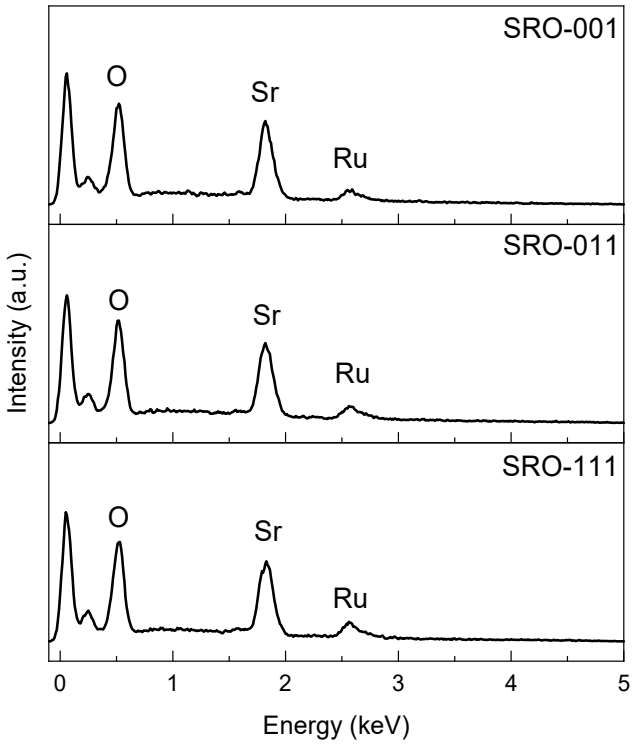

Figure S12: The EDX spectrum of SRO-001, SRO-011, and SRO-111.

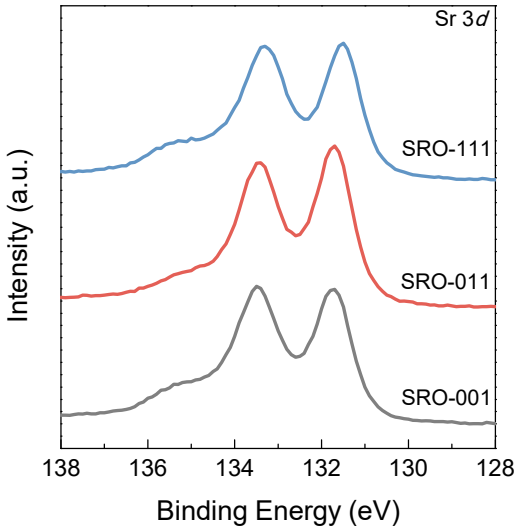

Figure S13: High-resolution XPS spectra of Sr 3*d* for SRO-001, SRO-011, and SRO-111.

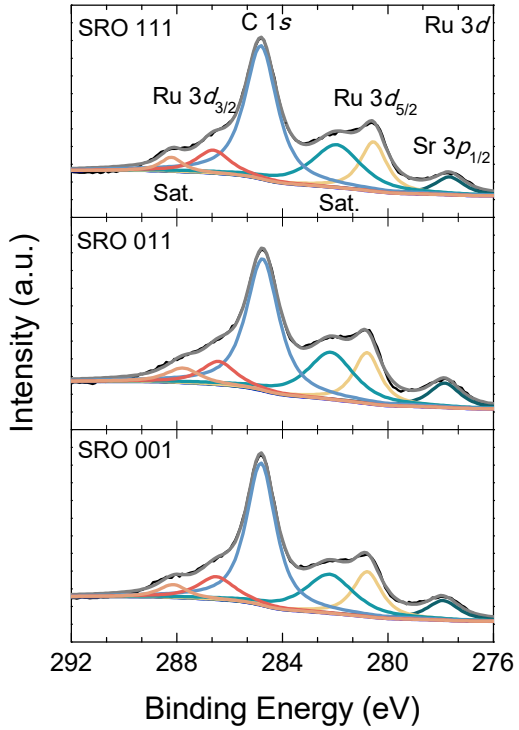

Figure S14: High-resolution XPS spectra of Ru 3*d* for SRO-001, SRO-011, and SRO-111.

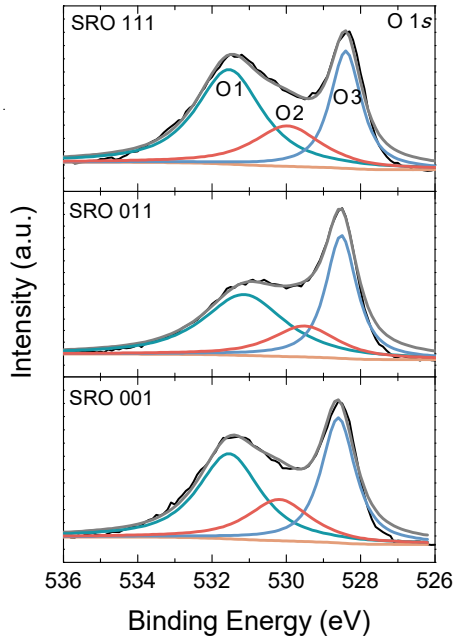

Figure S15: High-resolution XPS spectra of O 1*s* for SRO-001, SRO-011, and SRO-111.

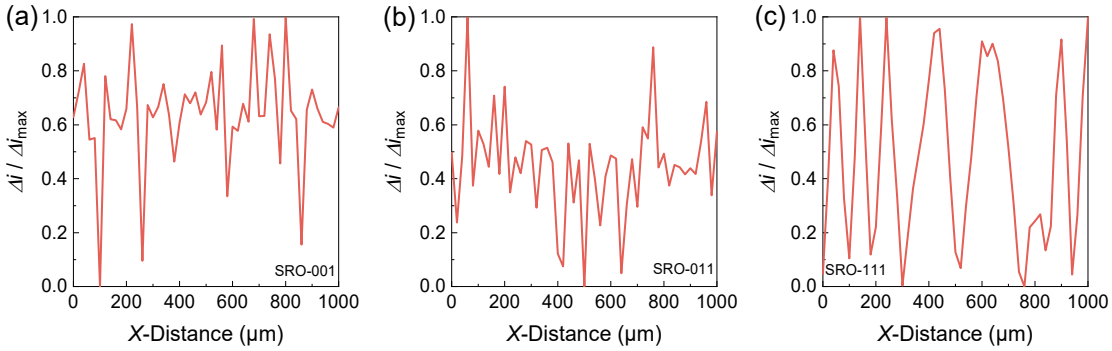

Figure S16: The normalized one-dimensional line scans of SECM at Y = 500 μm for SRO-001, SRO-011, and SRO-111.

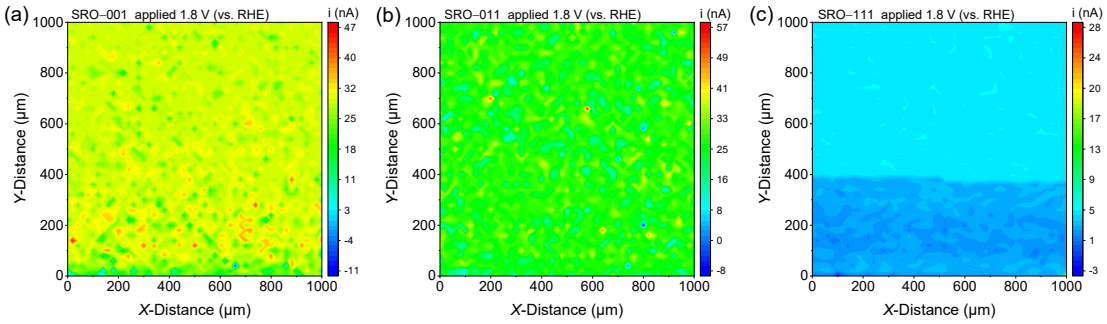

Figure S17: SECM images of OER performance at 1.8V for SRO-001, SRO-011, and SRO-111 without current normalization.

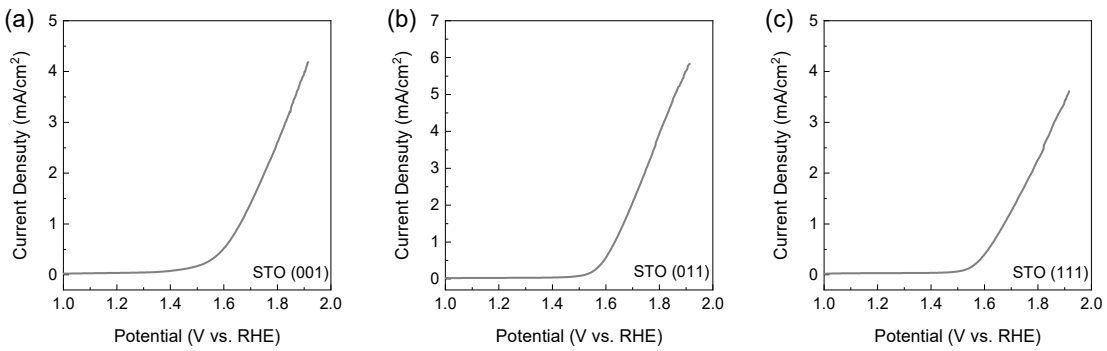

Figure S18: LSV curves of STO with different orientations. Steady-state LSV tests were conducted on STO substrates with different orientations to eliminate any interference from the substrate on the OER performance of the SRO thin films. Under the same testing conditions as the SRO thin films, the STO substrate exhibited only weak OER activity, with current densities of just 2-4 mA/cm² at 1.8 V. This indicates that the electrocatalytic influence of the substrate on the SRO thin films can be considered negligible during testing.

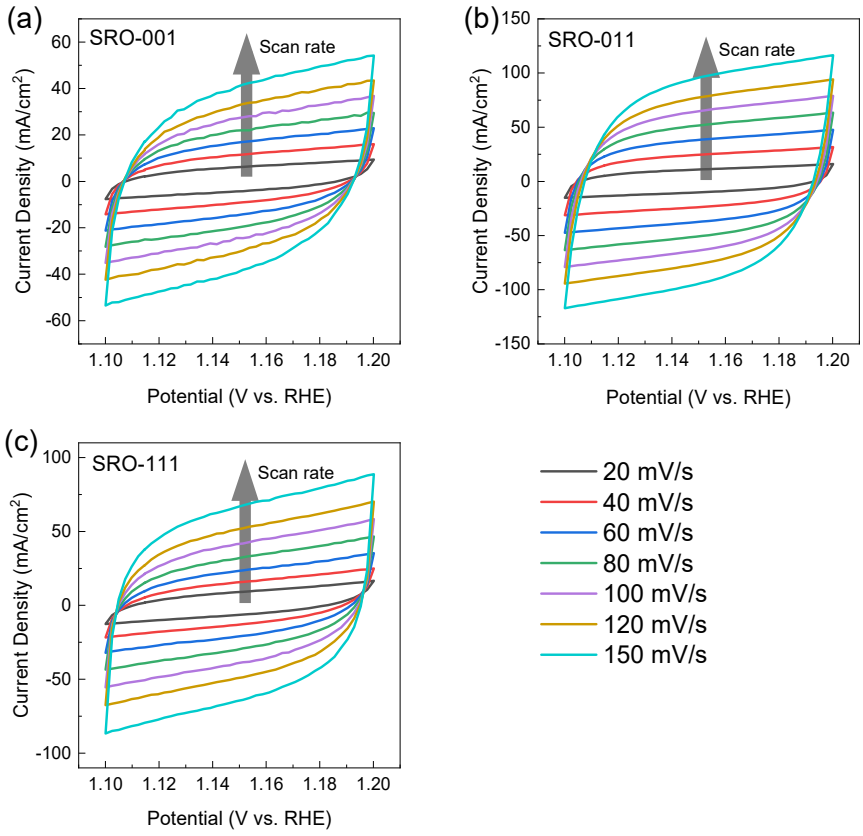

Figure S19: CV curves of SRO-001, SRO-011, and SRO-111.

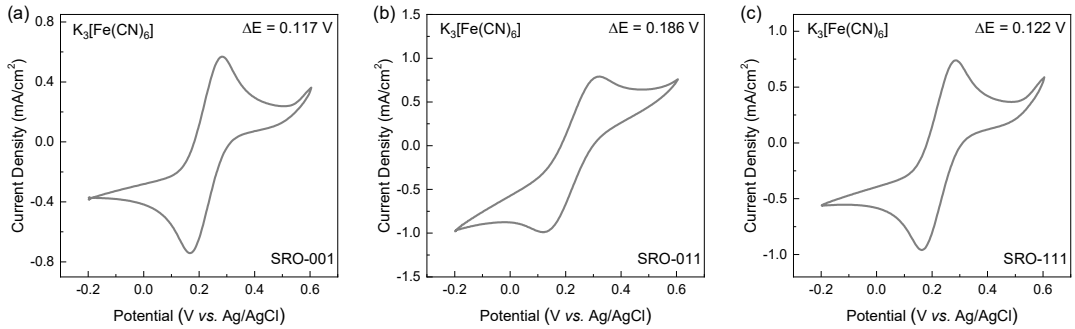

Figure S20: CV test of SRO-001, SRO-011, and SRO-111 in $K_3[Fe(CN)_6]$.

The results showed that the peak potential differences (ΔE) for the oxidation-reduction cycles are 0.117 V, 0.186 V, and 0.122 V for the SRO-001, SRO-011, and SRO-111 planes, respectively. These values indicate slight differences in charge transfer efficiency across different crystal facets, yet all maintain a relatively high level. The SRO-001 planes exhibiting somewhat more favorable electron transfer properties compared to the SRO-011 and SRO-111 plane. Furthermore, the peak currents for the oxidation and reduction reactions were found to be quite similar across all three planes, indicating a consistent electroactive area and comparable electrochemical behavior. DFT+U can only calculate the band properties of solids in an ideal state. The charge transfer characteristics of SRO in liquid solutions require analysis through electrochemical experiments, and the CV test precisely complements this deficiency.

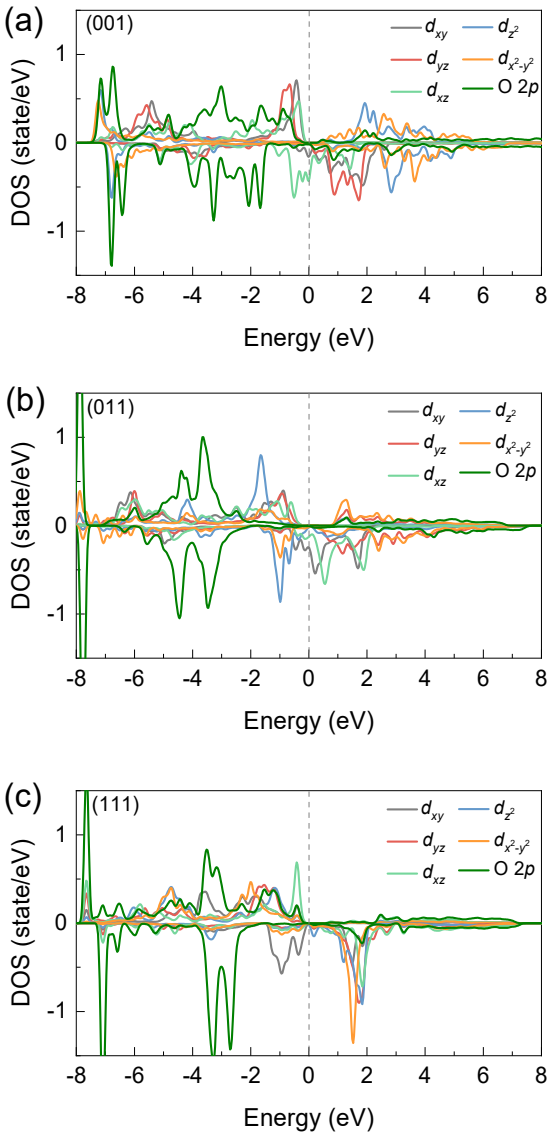

Figure S21: The PDOS of the Ru atom adsorbing OH species.

Table S9 Comparison of OER performance: this work *vs.* RuO_2 thin films

Film	Electrolyte	Current density (mA/cm^2)	Overpotential (mV)	Tafel slope (mV/dec)	Method
SRO (001), this work	1 M KOH	10 mA/cm^2	494	92	PLD
SRO (011), this work	1 M KOH	10 mA/cm^2	531	141	PLD
SRO (111), this work	1 M KOH	10 mA/cm^2	562	168	PLD
RuO_2 (101)[8]	0.1 M KOH	550 $\mu A/cm^2$	~ 330	/	MBE
RuO_2 (polycrystalline)[9]	1 M KOH	10 mA/cm^2	250	87	ALD

References

[1] J. P. Perdew, M. Ernzerhof, K. Burke, *J. Chem. Phys.* **1996**, 105, 9982.

[2] Kresse, Furthmuller, *Phys. Rev. B* **1996**, 54, 11169.

[3] G. Kresse, J. Furthmuller, *Comput. Mater. Sci.* **1996**, 6, 15.

[4] M. Kim, B. I. Min, *Phys. Rev. B* **2015**, 91, 205116.

[5] S. Grimme, *J. Comput. Chem.* **2006**, 27, 1787.

[6] J. K. Norskov, T. Bligaard, A. Logadottir, J. R. Kitchin, J. G. Chen, S. Pandelov, J. K. Norskov, *J. Electrochem. Soc.* **2005**, 152, J23.

[7] S. Pan, L. Zhang, M. Liu, X. Pan, M. Bi, T. Guo, Y. Zhang, J. Sun, A. Vasiliev, X. Ouyang, X. Wang, J. Zhu, Y. Fu, *ACS Sustainable Chem. Eng.* **2023**, 11, 290.

[8] P. Adiga, W. Nunn, C. Wong, A. K. Manjeshwar, S. Nair, B. Jalan, K. A. Stoerzinger, *Mater. Today Energy* **2022**, 28, 101087.

[9] J. Lee, S. Lee, Y. Kim, Y. Kwon, W. H. Kim, S. M. Chung, D. Kim, H. Kim, *Vacuum* **2024**, 220, 112843.